

Mapping the neutral atomic hydrogen gas outflow in the restarted radio galaxy 3C 236

R. Schulz¹, R. Morganti^{1,2}, K. Nyland³, Z. Paragi⁴, E. K. Mahony^{5,6}, and T. Oosterloo^{1,2}

¹ ASTRON, Netherlands Institute for Radio Astronomy, Postbus 2, 7990 AA, Dwingeloo, Netherlands
e-mail: schulz@astron.nl

² Kapteyn Astronomical Institute, University of Groningen, PO Box 800, 9700 AV Groningen, The Netherlands

³ National Radio Astronomy Observatory, Charlottesville, VA 22903, USA

⁴ Joint Institute for VLBI ERIC, Postbus 2, 7990 AA, Dwingeloo, Netherlands

⁵ Sydney Institute for Astronomy, School of Physics A28, The University of Sydney, NSW 2006, Australia

⁶ ARC Centre of Excellence for All-Sky Astrophysics (CAASTRO), Australia

–; –

ABSTRACT

The energetic feedback that is generated by radio jets in active galactic nuclei (AGNs) has been suggested to be able to produce fast outflows of atomic hydrogen (H I) gas that can be studied in absorption at high spatial resolution. We have used the Very Large Array (VLA) and a global very-long-baseline-interferometry (VLBI) array to locate and study in detail the H I outflow discovered with the Westerbork Synthesis Radio Telescope (WSRT) in the re-started radio galaxy 3C 236. We confirm, from the VLA data, the presence of a blue-shifted wing of the H I with a width of $\sim 1000 \text{ km s}^{-1}$. This H I outflow is partially recovered by the VLBI observation. In particular, we detect four clouds with masses of $0.28\text{--}1.5 \times 10^4 M_{\odot}$ with VLBI that do not follow the regular rotation of most of the H I. Three of these clouds are located, in projection, against the nuclear region on scales of $\lesssim 40 \text{ pc}$, while the fourth is co-spatial to the south-east lobe at a projected distance of $\sim 270 \text{ pc}$. Their velocities are between 150 and 640 km s^{-1} blue-shifted with respect to the velocity of the disk-related H I. These findings suggest that the outflow is at least partly formed by clouds, as predicted by some numerical simulations and originates already in the inner (few tens of pc) region of the radio galaxy. Our results indicate that all of the outflow could consist of many clouds with perhaps comparable properties as the ones detected, distributed also at larger radii from the nucleus where the lower brightness of the lobe does not allow us to detect them. However, we cannot rule out the presence of a diffuse component of the outflow. The fact that 3C 236 is a low excitation radio galaxy, makes it less likely that the optical AGN is able to produce strong radiative winds leaving the radio jet as the main driver for the H I outflow.

Key words. Galaxies: active - Galaxies: jets - Galaxies: individual: 3C 236 - Galaxies: ISM - Techniques: high angular resolution - ISM: jets and outflows

1. Introduction

The evolution of galaxies is considered to be strongly linked to that of their central supermassive black holes (SMBH). The required feedback is commonly explained by a phase of enhanced activity related to the SMBH (e.g., [Heckman & Best 2014](#); [Koromendy & Ho 2013](#)). An active galactic nucleus (AGN) can affect the interstellar medium (ISM) by heating-up and expelling gas which hinders star formation and the accretion of matter onto the SMBH (e.g., [Silk & Rees 1998](#); [Di Matteo et al. 2005](#); [Croton et al. 2006](#); [McNamara & Nulsen 2007](#)). Prominent observational signatures include outflows of ionized, molecular and atomic gas that have been associated with a number of AGN at a range of redshifts. The highest outflow rates have been determined for the cold ISM gas (molecular and atomic). Among the different possible drivers of these outflows are the radio jets launched in some AGN. The complex interplay between the AGN and the ISM requires detailed observational and theoretical studies of each phase of the outflowing gas (see reviews by [Veilleux et al. 2005](#); [Fabian 2012](#); [Alexander & Hickox 2012](#); [Wagner et al. 2016](#); [Tadhunter 2016](#); [Harrison 2017](#); [Morganti 2017](#) and references therein). Here, we focus on the outflows of neutral atomic hydrogen (H I) gas which have been observed in absorption in a number of radio sources with different radio

power (e.g., [Morganti et al. 1998, 2005b, 2013, 2016](#); [Oosterloo et al. 2000](#); [Mahony et al. 2013](#); [Geréb et al. 2015](#); [Allison et al. 2015](#)). Some of these objects host young or re-started AGN where the central radio source shows characteristics of a compact steep spectrum (CSS) object. This provides valuable insight into the evolution of radio galaxies, because CSS sources are considered to be the younger counterparts of the much larger Fanaroff-Riley type radio galaxies (e.g., [O’Dea 1998](#); [Kunert-Bajraszewska et al. 2010](#); [Oriente 2016](#)). The radio continuum is commonly a few kpc or less in size which limits the spatial scales on which the H I outflow can be observed. In the two radio galaxies 3C 305 and 3C 295, the outflows were found on kpc scales ([Morganti et al. 2005a](#); [Mahony et al. 2013](#)). However, in most cases sub-arcsecond angular resolution is needed in order to locate the outflow and trace its structure.

The angular resolution can be achieved by very long baseline interferometry (VLBI) which has been used to study the associated H I gas in absorption in various radio sources (e.g., [Carilli et al. 1998](#); [Peck et al. 1999](#); [Peck & Taylor 2001](#); [Vermeulen et al. 2003, 2006](#); [Struve & Conway 2010, 2012](#); [Araya et al. 2010](#)). The first detection of a broad H I outflow with VLBI was reported by [Oosterloo et al. \(2000\)](#) in the Seyfert 2 galaxy IC 5063. Of particular relevance for our study was the successful

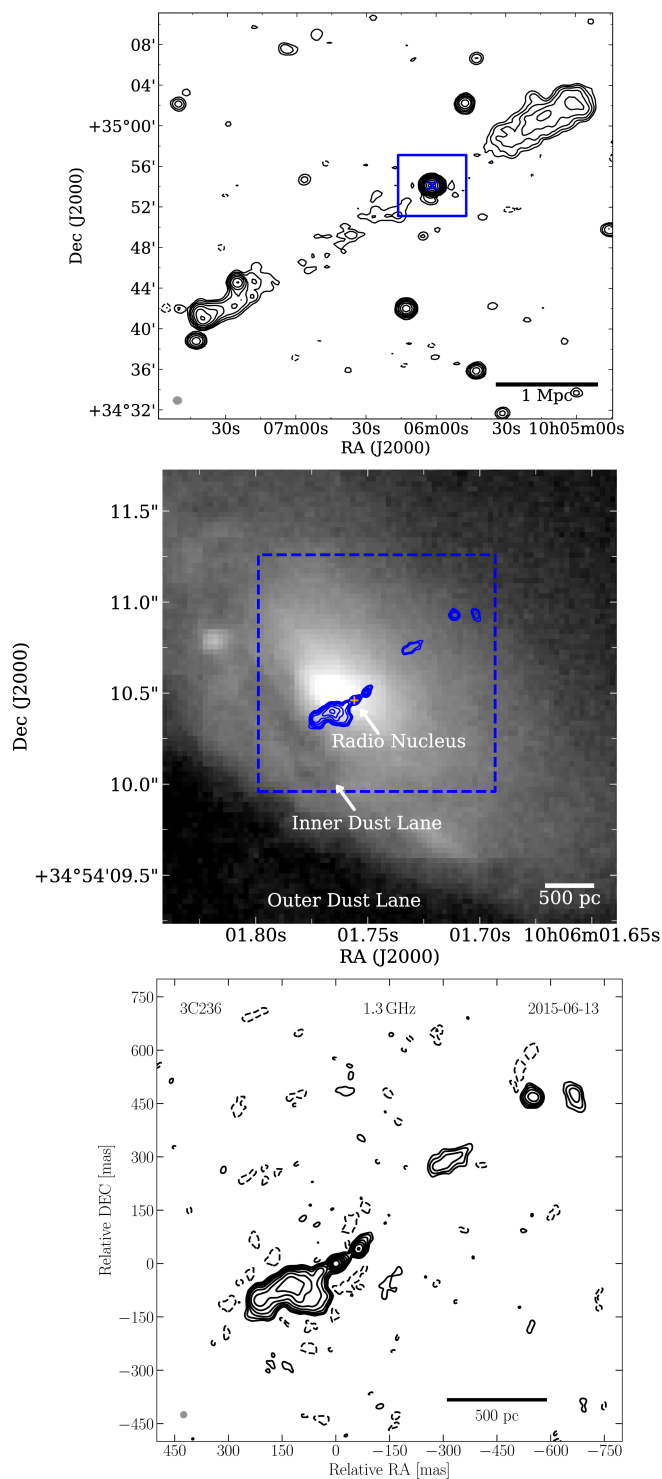


Fig. 1. Left panel: 1.4 GHz VLA NVSS image of the large-scale radio emission of 3C 236 (Condon et al. 1998). The blue square and cross highlight the area covered by our VLA observation and the pointing of the VLBI observation, respectively. Middle panel: the gray-colored background shows a zoom-in into archival *Hubble Space Telescope* V-band image (ACS/HRC/F555W, O’Dea et al. 2001). The blue contour lines trace the VLBI radio continuum emission starting for visibility at $5 \times \sigma_{\text{noise, VLBI}}$. The orange cross marks the position of the VLBI core from Taylor et al. (2001) to which our VLBI image was aligned to in this montage. The dashed lines mark the plot range of the VLBI image shown in the bottom panel. Bottom panel: VLBI image of obtained by our observation. The dashed and solid black contour lines trace negative and positive brightness starting from $3 \times \sigma_{\text{noise, VLBI}}$ and increasing logarithmically by a factor of 2.

imaging and mapping of the H I outflow in the young restarted radio galaxy 4C 12.50 by Morganti et al. (2013). The broad bandwidth and high sensitivity of the VLBI observation revealed the outflow in this source as an extended cloud co-spatial with the southern extent of the radio continuum emission. This is offset to the H I gas at the systemic velocity which is located north of the nucleus. The study determined a mass of the cloud of up to 10^5 solar masses (M_{\odot}) and a mass outflow rate of $16\text{--}29 M_{\odot} \text{ yr}^{-1}$. A comparison with an unresolved H I absorption spectrum obtained with the Westerbork Synthesis Radio Telescope (WSRT) showed that all of the absorption was recovered by VLBI. The results provide the strongest evidence for this type of radio AGN so far that the H I outflow is driven by the jet.

Based on these results, we performed VLBI observations of H I in absorption of a small sample comprising 3C 236, 3C 293, and 4C 52.37. This initial work will pave the way for future VLBI observations of H I gas in a larger sample selected from the WSRT H I absorption survey (Geréb et al. 2015; Maccagni et al. 2017).

In this paper, we focus on 3C 236 at a redshift of $z = 0.1005$ (Hill et al. 1996) which is one of the largest known radio galaxies extending about 4.5 Mpc (Willis et al. 1974; Barthel et al. 1985; Schilizzi et al. 2001). This source represents a re-started AGN, i.e., it exhibits signs of different stages of AGN activity. The large scale morphology (top panel in Fig. 1) stems from a previous cycle of activity compared to the CSS-type radio source in its inner 2 kpc region which is the result of the most recent cycle. The inner radio emission has a dynamical time scale consistent with the age of the young star formation region (O’Dea et al. 2001; Schilizzi et al. 2001; Tremblay et al. 2010).

The host galaxy of 3C 236 features a large outer and a smaller inner dust lane which are slightly offset in position angle (PA) with respect to each other (O’Dea et al. 2001; Schilizzi et al. 2001; Labiano et al. 2013). The inner dust lane has a PA of $\sim 30^{\circ}$ which is almost perpendicular to the sub-kpc scale radio jet. VLBI observations by Schilizzi et al. (2001) showed that the jet is oriented in north-west direction extending from the brightest feature which is synchrotron self-absorbed and thus likely to be the core region. The south-east lobe produced by the counter jet is positionally coincident with parts of the inner dust lane and its morphology is considered to be partially a result of jet-ISM interaction. The background image in the middle panel of Fig. 1 shows a zoom-in of the inner dust lane overlaid by the brightness distribution of the radio source as obtained in this paper (bottom panel of Fig. 1, see Sect. 3).

Low-resolution H I absorption spectra reveal a deep narrow absorption feature near the systemic velocity (van Gorkom et al. 1989) and a broad (up to 1000 km s^{-1}) shallow blue wing corresponding to a mass outflow rate of $\sim 47 M_{\odot} \text{ yr}^{-1}$ (Morganti et al. 2005b). Based on H I VLBI observations by Struve & Conway (2012), the narrow component has been interpreted as H I gas located in a regular rotating disk which is co-spatial to the south-east lobe about 250 mas from the nucleus. Because of bandwidth limitations the VLBI data was not able to cover the velocity range of the outflow.

The optical AGN has been classified as a low-excitation radio galaxy (LERG, Buttiglione et al. 2010; Best & Heckman 2012) which makes it less likely that strong quasar or starburst-driven winds are the origin of the outflow, but rather the jets. There are also signs of an outflow of ionized gas (Labiano et al. 2013). The cold (CO) and warm (H_2) molecular gas have only been detected in a disk-like geometry aligned with position angle of the inner dust lane, but the latter has a significant turbulent component (Nesvadba et al. 2011; Labiano et al. 2013).

This paper presents new VLBI observations with a larger bandwidth than previous data to localise the H I outflow with respect to the radio jet and constrain its properties in combination with new lower resolution Very Large Array (VLA) data. It is structured as follows: in Sect. 2 we present the data and subsequent calibration procedure. This is followed by a presentation of our results in Sect. 3 and discussion in Sect. 4. We end the paper with our conclusions and a summary in Sect. 5.

Throughout this paper, we adopt a standard Λ CDM-cosmology ($H_0 = 70 \text{ km s}^{-1} \text{ Mpc}^{-1}$, $\Omega_m = 0.3$, $\Omega_\lambda = 0.7$) based on which 1.0 mas corresponds to about 1.8 pc for 3C 236. It is important to point out that a range of values are available for the systemic velocity v_{sys} (see also [Struve & Conway \(2012\)](#)). [Labiano et al. \(2013\)](#) determined $v_{\text{sys}}^{\text{CO}} \approx 29761 \text{ km s}^{-1}$ based on the CO spectrum, though the spectral setup prohibited sampling of the continuum emission at low velocities limiting the Gaussian fit to the spectrum. Nevertheless, this value is close to the SDSS value of $v_{\text{sys}}^{\text{SDSS}} \approx 29740 \text{ km s}^{-1}$. [Struve & Conway \(2012\)](#) reported a value of $v_{\text{sys}}^{\text{H I}} \approx 29820 \text{ km s}^{-1}$ assuming that parts of the observed H I is constrained within a disk. However, the H I was detected in absorption which makes it difficult to measure the full extent of the disk (see also Sect. 4.2). Therefore, we use $v_{\text{sys}}^{\text{CO}}$ throughout this paper as a reference value.

2. Observation & Data reduction

2.1. VLBI Observation

3C 236 was observed with a global VLBI array of 14 telescopes on 2015 Jun 13 (project code: GN002B). The observational setup is summarized in Table 1. The array included the full VLBA and stations from the European VLBI Network (EVN). In addition, Arecibo (Puerto Rico) participated for two hours. The observation lasted a total of 15 hours with the EVN and VLBA observing for ~ 11 hours and ~ 12 hours, respectively, and including an overlap between both arrays of ~ 8 hours. The stations of Onsala and Kitt Peak (VLBA) were flagged during the calibration due to unusually high system temperatures and bandpass problems, respectively. The data were correlated at the Joint Institute for VLBI ERIC (JIVE) providing two data sets, i.e., one with 4 IFs each with 32 channels (‘continuum pass’) and one with one IF with 512 channels (‘spectral-line pass’). 0958+346 (BZQ J1001+3424) was observed as the phase reference calibrator, while 0955+326 (3C 232) and 0923+392 ([HB89] 0923+392) served as the bandpass calibrators.

The data were calibrated in two steps using standard procedures in the Astronomical Image Processing Software (AIPS, version 31DEC15) package ([Associated Universities 1999](#)) and beginning with the data from the continuum pass. The amplitude calibration and initial flagging were provided by the EVN pipeline. As a next step manual phase calibration on a single scan of the calibrator was performed to remove the instrumental delay. This was followed by a global fringe fit of the calibrators to correct for the phase delay and rate with the solutions applied to the target source. Finally, the bandpass was corrected using the bandpass calibrators and the solutions applied to the phase reference and target source. For the spectral-line pass, the amplitude calibration and initial flagging was also taken from the EVN pipeline. The phase calibration was performed using the solutions from the manual phase calibration and global fringe fit of the continuum pass, which was followed by the bandpass calibration. Afterwards, the data were separated into a data cube with full spectral resolution and continuum data set with all channels averaged together.

The continuum data were further processed in DIFMAP ([Shepherd et al. 1994](#); [Shepherd 2011](#)). This entailed imaging of the brightness distribution of the source using the CLEAN-algorithm ([Högbom 1974](#)) in combination with phase self-calibration and flagging of corrupted visibilities. Once a sufficiently good model was found, a time-independent gain correction factor was determined for each telescope through amplitude self-calibration. The iterative process of imaging and phase self-calibration with subsequent time-dependent amplitude self-calibration was repeated several times with decreasing solution interval for amplitude self-calibration.

The resulting continuum image was used to perform a single phase self-calibration of the data cube with full spectral resolution in AIPS. After carefully inspecting the channels and flagging of corrupted visibilities, the continuum was subtracted in the visibility domain using a linear fit to the first and last 100 channels (AIPS task UVLIN). Since we focus on the faint and broad component of the absorption, we averaged over three consecutive channels to improve the sensitivity. The data were corrected for the Doppler shift in frequency caused by the rotation and movement of the Earth. Finally, a redshift correction was applied to the channel width in observed frequency to convert into rest-frame velocity following [Meyer et al. \(2017\)](#).

Each channel of the spectral-line cube was imaged individually with robust weighting set to 1 and a (u, v) -taper of $10 \text{ M}\lambda$ to further improve the sensitivity. We found that this tapering of the visibility data provides the best combination of resolution and sensitivity. It is similar to [Struve & Conway \(2012\)](#). The channels were only imaged if significant negative flux density was found in the area covered by continuum emission. The resulting cube covers a velocity range of $28117\text{--}31209 \text{ km s}^{-1}$ at channel resolution of 21.7 km s^{-1} which is effectively doubled to 43.4 km s^{-1} due to Hanning-smoothing.

In order to compare the image cube and the continuum image, both were restored with the same circular restoring beam of 20 mas. This is close to the synthesized beam due to the (u, v) -tapering and similar to [Struve & Conway \(2012\)](#). The noise levels were determined by fitting a Gaussian distribution to the pixels which are not contaminated by emission from the target following the procedure outlined in [Böck \(2012\)](#). For the subsequent analysis the average noise level of the cube is used as a reference value. An overview of the image parameters is given in Table 2. The overall amplitude calibration uncertainty of the VLBI data was estimated to be around 15% based on multiple iterations of imaging and self-calibration of the continuum data. The total flux density was measured in the image plane using the CASA Viewer ([International Consortium Of Scientists 2011](#)). We estimated the uncertainty of the peak and total flux density measurement as $\sqrt{(N_{\text{beam}} \times \sigma_{\text{noise}})^2 + (0.15 \times S_{\text{tot}})^2}$ following [Nyland et al. \(2016\)](#) where N_{beam} corresponds to the number of beams covered by the source. However, we noticed that in our case the first term has only a marginally impact on the uncertainty.

2.2. VLA Observation

The VLA observed 3C 236 for 40 min in A-array configuration (project code: 11A-166) on 2011 Aug 10. The setup is summarized in Table 1. 1328+307 (3C 286) was used as the flux density calibrator and 1015+359 (B2 1015+35B) as the complex gain calibrator.

The data were processed with MIRIAD ([Sault et al. 1995, 2011](#)). Due to technical difficulties one polarisation was lost and

Table 1. Properties of Observations

Array ^a	Code ^b	Date	ν_{obs}^c [GHz]	T_{obs}^d [min]	Pol. ^e	Correlator Pass	IFs [MHz]	BW ^f	N_{ch}^g [kHz]	$\Delta\nu^h$
EVN+VLBA+Ar	GN002B	2015-06-13	1.293	500	Dual	continuum spectral-line	4 1	16	32 512	500 31.25
VLA	11A-166	2011-08-10	1.283	40	Dual	spectral-line	1	16	256	62.5

Notes. ^(a) Array used for observation. EVN: Effelsberg (Germany), phased-up Westerbork (5 stations, Netherlands), Jodrell-Bank (United Kingdom), Onsala (Sweden); VLBA (USA): Los Alamos (NM), Kitt Peak (AZ), St. Croix (VI), Mauna Kea (HI), Hancock (NH), Brewster (WA), Fort Davis (TX), North Liberty (IA), Pie Town (NM), Owens Valley (CA); Ar: Arecibo (Puerto Rico). ^(b) Experiment Code ^(c) Observing frequency ^(d) Observing time. For the VLBI experiment, this represents the total on source time of the whole array. ^(e) Polarization: Dual refers to two polarization were used (LL and RR) ^(f) Bandwidth (of each IF) ^(g) Number of channels in a single band or IF ^(h) Channel width in frequency

Table 2. Properties of Images

Data	σ_{noise}^a [mJy beam ⁻¹ ch ⁻¹]	Beam ^b	$\Delta\nu^c$ [km s ⁻¹]	N_{ch}^d	S_{peak}^e [Jy beam ⁻¹]	S_{tot}^f [Jy]
VLBI						
Continuum	0.23	20mas × 20mas	-	1	0.145 ± 0.020	1.35 ± 0.20
Cube	0.37	20mas × 20mas	21.7 (43.4)	143	-	-
VLA						
Continuum	2.1	1''7 × 1''2, -67°	-	1	2.883 ± 0.086	3.37 ± 0.10
Cube (VLBI)	1.1	2''0 × 1''5, -81°	21.7 (43.4)	157	-	-
Cube (WSRT)	1.1	2''0 × 1''5, -81°	20.0 (40.0)	186	-	-

Notes. ^(a) Noise level. For the cubes, this value represents the average value over all channels ^(b) Synthesized beam as major axis, minor axis and the position angle ^(c) Channel width in velocity of the cubes after re-sampling. The value in brackets corresponds to the effective resolution after Hanning-smoothing ^(d) Number of channels of the cubes ^(e) Total flux density of the continuum image ^(f) Peak flux density of the continuum image

had to be flagged completely. The data were calibrated using standard procedures for the VLA. A continuum image was produced using CLEAN and self-calibration. The spectral-line data were continuum subtracted using only channels devoid of the broad absorption. Further processing was performed in AIPS. The VLA cube was averaged to match the velocity resolution of the VLBI data, cleaned in the region of the continuum emission and afterwards Hanning smoothed. Consistent with the VLBI spectral-line data, the channel width was redshift-corrected to the rest-frame velocity width. The resulting image cube covers a velocity range from (28316–31706) km s⁻¹. For a comparison with the WSRT spectrum presented in [Morganti et al. \(2005b\)](#), we also created a second cube which matches the velocity resolution of the WSRT data. The parameters of the continuum image and the cube are given in Table 2. We estimate the uncertainty of the absolute flux density scale at this frequency and given the calibrators to be ~ 3% based on ([Perley & Butler 2013](#)).

3. Results

3.1. VLA and VLBI continuum

The VLA continuum image covers the central 6' × 6' (650 kpc × 650 kpc) of 3C 236 (see Fig. 1). The recovered radio emission is unresolved and yields a flux density of about 3.37 ± 0.10 Jy. No further extended emission is detected. The flux density is consistent with the value of 3.324 ± 0.097 Jy obtained from the central region of the radio emission by the lower-resolution NVSS survey at 1.4 GHz ([Condon et al. 1998](#)). The full VLBI continuum emission of 3C 236 from our observation is shown in the bottom panel of Fig. 1. The total flux density is about 1.35 ± 0.20 Jy which is consistent with the value obtained by [Struve & Conway \(2012\)](#) (1.36 Jy). It corresponds to about 40% of the flux density measured by the VLA observation. The source is significantly

extended covering approximately 1'' (~ 1.8 kpc), but most of the radio emission is localized within 400 mas (~ 720 pc).

The difference in flux density between VLBI and VLA of about 2 Jy can have different reasons. Firstly, the shortest baseline of the VLBI array limits the largest angular scale on which emission can be recovered to about 600 mas. Any extended emission on larger scales is resolved out by the interferometer. However, there could still be a significant amount of emission within the largest angular scale limit. Assuming the emission is uniformly distributed over the entire area, then an integrated flux density of more than 600 mJy is necessary to achieve a brightness at the $3\sigma_{\text{VLBI,cont}}$ sensitivity limit of the VLBI image. Secondly, the consistency between our VLA and the NVSS flux density shows that all of the undetected emission must be within the area covered by the synthesized beam of the VLA observation, i.e. 1''7 × 1''2 (3.1 kpc × 2.2 kpc). Assuming again a uniform distribution of the undetected emission over this region leads to a brightness of about 0.6 mJy beam⁻¹. This is just below the $3\sigma_{\text{VLBI,cont}}$ -limit. Thus, a global VLBI experiment including the VLA and eMERLIN would provide the sensitivity and short spacing to recover all of the emission.

The morphology is overall consistent with previous VLBI observations by [Schilizzi et al. \(2001\)](#) and [Struve & Conway \(2012\)](#). The sensitivity of our VLBI image is about a factor of three better than the image from [Struve & Conway \(2012\)](#), but we do not detect significantly more extended emission or any movement of features in the jet at the given resolution. Following [Schilizzi et al. \(2001\)](#), we consider the location of the VLBI core region to coincide with the brightest feature at the phase center of the image and the jet to extend to the north-west. The emission in the south-east direction from the core region corresponds to the radio lobe created by the counter jet. Due to the chosen restoring beam, the brightest feature is actually a blend of the emission from the VLBI core and part of the innermost jet.

We refer to this as the nuclear region from here on. In the following, we continue to focus on the inner most 400 mas of the source where the bulk of the radio emission is located. We determine the position angle of the jet as the angle along which the brightest features of the south-east jet are best aligned on to be about 116° which is consistent with the measurement of [Struve & Conway \(2012\)](#) of 117° .

3.2. H I absorption spectrum

Figure 2 (top panel) shows the unresolved VLA spectrum between 28500 km s^{-1} and 30900 km s^{-1} in combination with the WSRT spectrum from [Morganti et al. \(2005b\)](#). The spectra taken with both instruments are consistent and show the same features, i.e., a deep and narrow absorption that smoothly falls off towards higher velocities, but has a complex, broad wing towards lower velocities. The consistency between both spectra implies that all of the absorption stems from scales smaller than the beam size of the VLA.

Two spatially integrated VLBI spectra are shown in the bottom panel of Fig. 2 between 29000 km s^{-1} and 30400 km s^{-1} . Both were compiled by considering those pixels in the image cube that are located within the region marked by the $3\sigma_{\text{VLBI,cont}}$ contour line of the continuum image. They differ in terms of the selection of pixels in the cube. For the dashed, blue line labelled ‘VLBI (clipped)’ a very conservative limit of $|S_{\text{pixel,cube}}| \geq 3 \times \sigma_{\text{VLBI,cube}}$ was used where $|S_{\text{pixel,cube}}|$ is the absolute value of the pixel brightness. No such limit was applied for the compilation of the spectrum marked by the solid, blue line (labelled ‘VLBI’) and the VLA spectrum (solid, red line) which is unresolved in contrast to the VLBI spectrum.

The VLBI without clipping shows a deep and narrow absorption feature consistent with the previous measurement by [Struve & Conway \(2012\)](#), but its depth and width does not match the VLA reference spectrum. Because the deep absorption is likely due to gas associated with the extended dust lane (see Sect. 3.3), the undetected absorption flux density is likely related to structure resolved out as seen from the missing continuum flux density. However, some unsettled gas appears in our VLBI observations (see Sect. 3.3). More interesting, the observations reveal some of the outflowing gas (bottom panel of Fig. 2). However, the VLBI observation recover only a small fraction of the blue-shifted wing of the H I profiles. We will discuss the possible implications of this for the distribution of the outflowing gas in Sect. 4.1.

3.3. H I gas distribution

The spatial distribution of the H I gas is shown in the central panel of Fig. 3. It shows the optical depth τ integrated over the same velocity range as in the bottom panel of Fig. 2, i.e., between 29000 km s^{-1} and 30400 km s^{-1} . The optical depth is defined as $\tau = \log(1 - \Delta S_{\text{abs}}/(c_f S_{\text{cont}}))$ where ΔS_{abs} and S_{cont} correspond to the absorbed and the continuum flux density, respectively, and the covering factor c_f is assumed to be unity. In order to avoid integrating over noise and to get a reliable albeit conservative distribution of the H I gas, we take into account only channels with $\leq -3\sigma_{\text{VLBI,cube}}$. In addition to the integrated optical depth $\int \tau dv$, this figure shows single-pixel spectra of optical depth extracted at specific locations of the radio continuum, for which the detection limit of channels was not applied.

The map of $\int \tau dv$ reveals a complex gas distribution across the south-east lobe and compact absorption towards the nucleus.

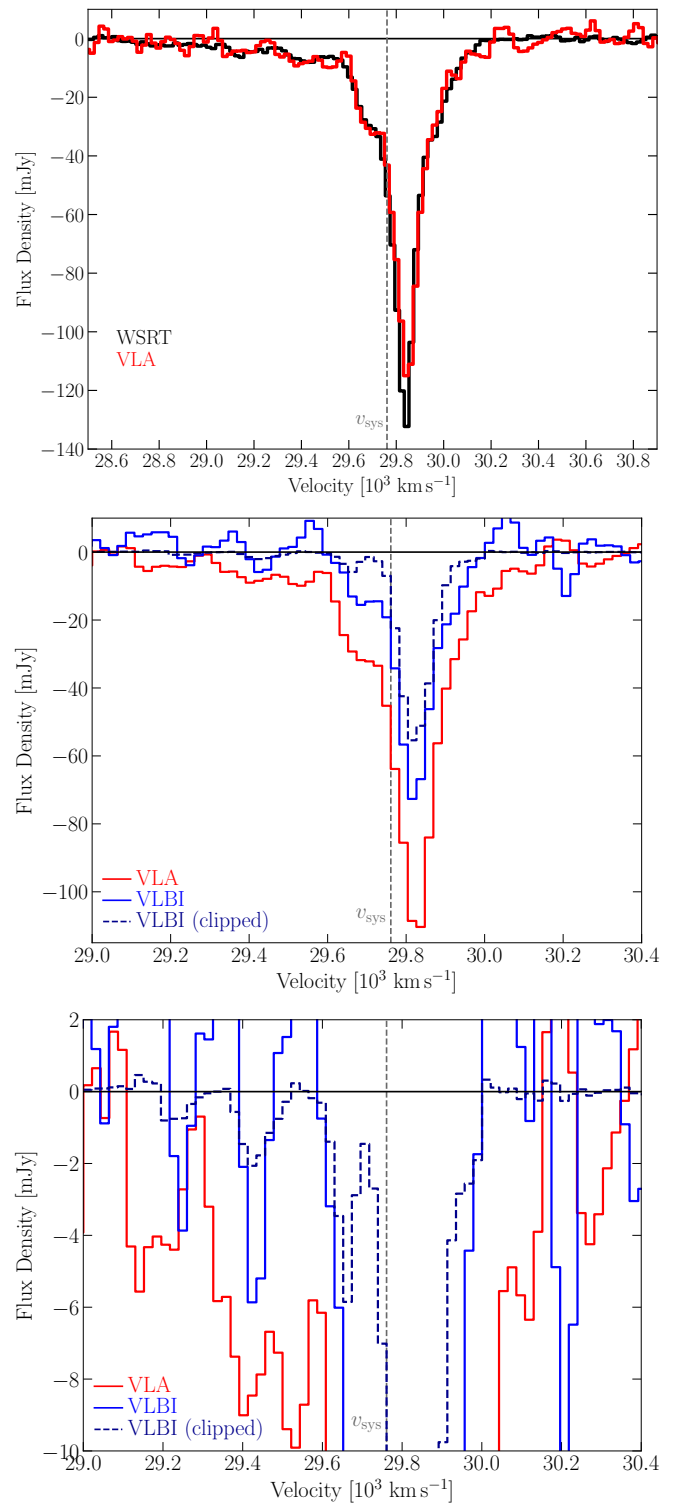


Fig. 2. H I absorption spectra of 3C 236. The dashed, vertical line marks the systemic velocity from [Labiano et al. \(2013\)](#). Top panel: WSRT (black) spectrum from [Morganti et al. \(2005b\)](#) and VLA (red) spectrum between 28500 – 30900 km s^{-1} . Here, the velocity resolution of the VLA spectrum was matched to the WSRT data. Middle panel: The spatially integrated VLBI with (darkblue, dashed) and without (blue, solid) clipping of the cube pixels at the $3\sigma_{\text{VLBI,Cube}}$ between 29000 – 30400 km s^{-1} . For the VLA spectrum (red), the spectral resolution was matched to the VLBI spectrum. Bottom panel: Same as the middle panel, but zoomed-in in flux density.

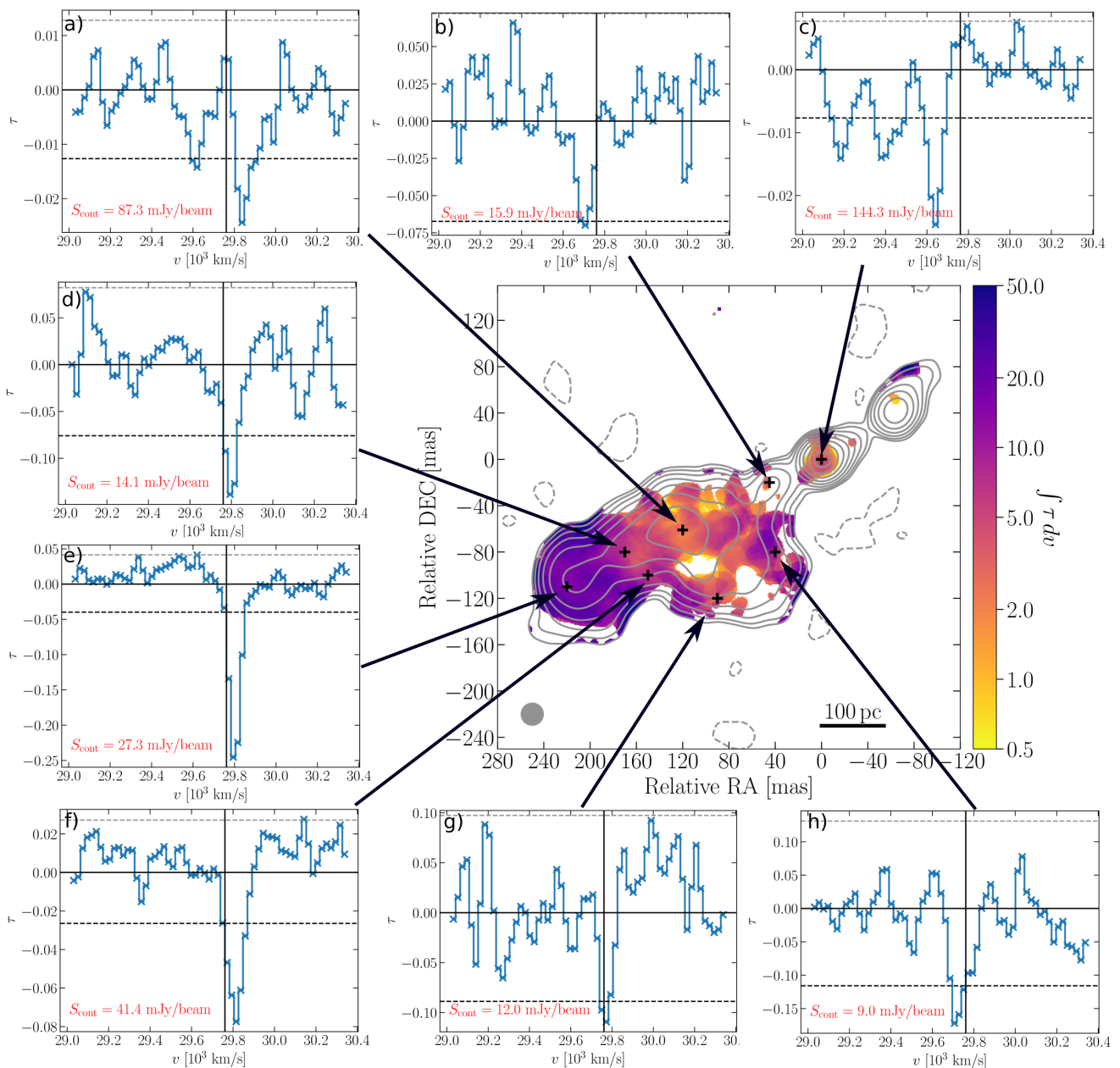


Fig. 3. Central panel: Continuum image of the central region of 3C236 shown in Fig. 1. The contour lines start at $3\sigma_{\text{VLBI,cont}}$ and increase logarithmically by a factor of 2. Solid and dashed contour lines correspond to positive and negative flux density, respectively. The black crosses mark areas where the spectrum was extracted between 29000–30000 km s^{-1} . Outer panels: The optical depth spectrum shown as the ratio of the absorbed flux density to the continuum flux density. The dashed line represents the optical depth detection limit at the $3\sigma_{\text{VLBI,cube}}$ -noise level. The solid, vertical line marks the systemic velocity.

In particular, the gas covering the south-east lobe exhibits significant changes in $\int \tau dv$. In the central and brightest part of the lobe $\int \tau dv$ reaches its lowest values, but there are several gaps in the gas distribution, in particular towards the nuclear region. The highest values of $\int \tau dv$ are measured towards the end of the south-east lobe. This is the region where the majority of the HI gas leading to the narrow, deep feature in the integrated spectrum, is situated.

The spectra of τ in Fig. 3a–h shows the range of optical depth probed by our observation. The lowest optical depth is reached towards the nuclear region as it has the brightest part of the radio source (Fig. 3c). Here, we are sensitive down to $\tau \geq 0.0077$ at the $3\sigma_{\text{VLBI,cube}}$ -noise level and find three distinct kinematic features

which will be discussed in greater detail later in this section. Towards the south-east lobe, the optical depth sensitivity varies. The lowest optical depth is reached in the central region of the lobe (Fig. 3a) with $\tau \gtrsim 0.013$ where we also find a more complex kinematic structure than in the other regions.

In order to investigate the spatial and velocity distribution of these features in greater detail, we show position-velocity plots along different position angles in Fig. 4a–e. Again, we focus on the velocity range of 29000 km s^{-1} and 30400 km s^{-1} . For comparison, the central panel shows the same map of $\int \tau dv$ as in Fig. 3.

Figure 4c and d show the velocity structure of the gas along the jet position angle and along the position angle of the inner dust lane, respectively. In particular, Fig. 4d reveals a gradient in velocity similar to [Struve & Conway \(2012\)](#) which has been interpreted as a signature of an H I disk aligned with the inner dust lane. Our new data shows that this gradient is even more prominent across the central part of the lobe (Fig. 4e). At the $-2\sigma_{\text{VLBI,cube}}$ -level, the gradient would cover almost 300 km s^{-1} . We label the disk-related feature in the following as S1.

However, more interesting and relevant from these observations are structures that appear to have a disturbed kinematics (see Figure 4c). S2b is located towards the central part of the lobe and is slightly blue-shifted with respect to the peak of the absorption by about 150 km s^{-1} . At the $3\sigma_{\text{VLBI,cube}}$ -level it is not connected to S1 spatially or in velocity. The clear separation in velocity between S2b and S1 could indicate that S2b traces a different component of the H I gas than S1.

The most important result from the new observations is the finding that the gas co-spatial to the nucleus is entirely blue-shifted with respect to the peak absorption by up to $\sim 640 \text{ km s}^{-1}$ (Fig. 4a,c). The projected size of this region is only about 36 pc or even smaller. It comprises three distinct features labelled S2a, S3, and S4, which are separated in velocity by a few channels. While it is possible that this separation could be due to changes in sensitivity across the channels, we consider this to be the least likely explanation as the variation in sensitivity are not significant. This leaves three other possibilities (see also Sect. 4.1). First, there is no further H I gas in this region or the optical depth of the gas is too low to be detectable. In this case the majority of the remaining outflowing gas would have to be located elsewhere. Second, the cold H I gas clouds could be entrained by warmer H I gas which has a higher spin temperature and thus, a lower optical depth. Third, the gas within the outflow is highly clumpy which could imply differences in the covering factor or spin temperature of the gas.

We cannot exclude the possibility of H I gas co-spatial to the north-west part of the jet. Figure 4b and the map of $\int \tau dv$ suggest that there could be gas in this region that is redshifted with respect to the deep absorption. However, these features are just at the $3\sigma_{\text{VLBI,cube}}$ -level, very narrow and generally located at the edge of the continuum emission. Therefore, we cannot consider them reliable detections.

4. Discussion

Our VLBI observation has successfully recovered part of the outflowing H I gas in 3C 236 in the form of distinct, compact clouds (S2a, S3, S4). They are located primarily co-spatial, in projection, to the nuclear region which has a projected size of $\lesssim 36 \text{ pc}$ with one possible exception (S2b). The clouds cover velocities of $150\text{--}600 \text{ km s}^{-1}$ blue-shifted with respect to the H I that is likely related to a rotating disk aligned with inner dust lane (S1). The

disk-related gas extends over most over the south-east radio lobe. The overall gas distribution is clumpy with the majority of the gas concentrated at the end of the lobe. An important characteristic of the H I VLBI data is the significant amount of H I absorption that is not detected, but inferred from low-angular resolution observations with the VLA and the WSRT.

4.1. The high-velocity H I gas

As mentioned in Sect. 1, 3C 236 is classified as a LERG, which makes it less likely that the AGN is able to produce powerful radiative winds which could couple to the dust of the galaxy and create strong gaseous outflows. This in turn leaves the radio jet as the main driver for the H I outflow, i.e., features S2a, S3, S4, and perhaps S2b. However, we cannot exclude the possibility of S2b being part of the H I disk (see also Sect. 4.2).

The location of S2a, S3, and S4 suggests that the outflow starts already very close to the nucleus of 3C 236 (see also Fig. 5a, b, and c). As these structures are unresolved, we use the restoring beam as an upper limit of the extent of the H I gas ($\lesssim 36 \text{ pc}$ in projection). In contrast, S2b is extended and we estimate its projected size to be about $54 \text{ pc} \times 15 \text{ pc}$.

There are several implications for the undetected absorbed flux density in our VLBI observation. The diffuse extended continuum emission that is resolved out by the high-resolution of VLBI (see Section 3.1) limits the area over which we can probe for absorption. However, we could still be able to detect H I absorption in regions outside of the detected continuum emission if the absorption is compact. In fact, in some channels the absorption does extend marginally outside of the $3\sigma_{\text{VLBI,cont}}$ contour lines, but is below the $3\sigma_{\text{VLBI,cube}}$ -level.

Another possibility is related to the small fraction of the outflow detected only against the nuclear region. This region is the brightest one with a peak flux density of about 145 mJy which corresponds to an optical depth limit of 0.0026 at the $1\sigma_{\text{VLBI,cube}}$ -level or 0.0077 at the $3\sigma_{\text{VLBI,cube}}$ -level. It is worth noting that some of the channels between S4 and S3 and between S3 and S2a have optical depths above the $1\sigma_{\text{VLBI,cube}}$ -level at the location of the peak continuum flux density. However, the peak flux density of the lobe is about 87 mJy, which corresponds to an optical depth limit of 0.0043 at the $1\sigma_{\text{VLBI,cube}}$ -level or 0.013 at the $3\sigma_{\text{VLBI,cube}}$ -level. The peak optical depth of the clouds S3 and S4 is about 0.014 which is consistent with the $3\sigma_{\text{VLBI,cube}}$ -level within in our amplitude calibration uncertainty. Thus, we cannot entirely exclude the existence of clouds such as S3 and S4 at larger distances from the nucleus, i.e., against the lobe. However, we cannot detect these clouds because of sensitivity limits.

This could be a likely situation and entails that the outflow is actually more extended but made up of clouds similar to the one detected against the nucleus. We cannot exclude a component of diffuse gas, but this would be also too faint to be detectable. We can exclude the presence of single clouds producing a depth of the absorption similar to the one detected by the VLA and WSRT (see Fig. 2). Taking the peak flux density of the lobe and the lowest absorption recovered by the WSRT at around 28800 km s^{-1} would correspond to an optical depth of 0.02. Therefore, such clouds would have been detected at least against the brighter part of the lobe. We would also not have seen this cloud towards the nuclear region, the peak flux density implies an optical depth of about 0.015 similar to S3 and S4.

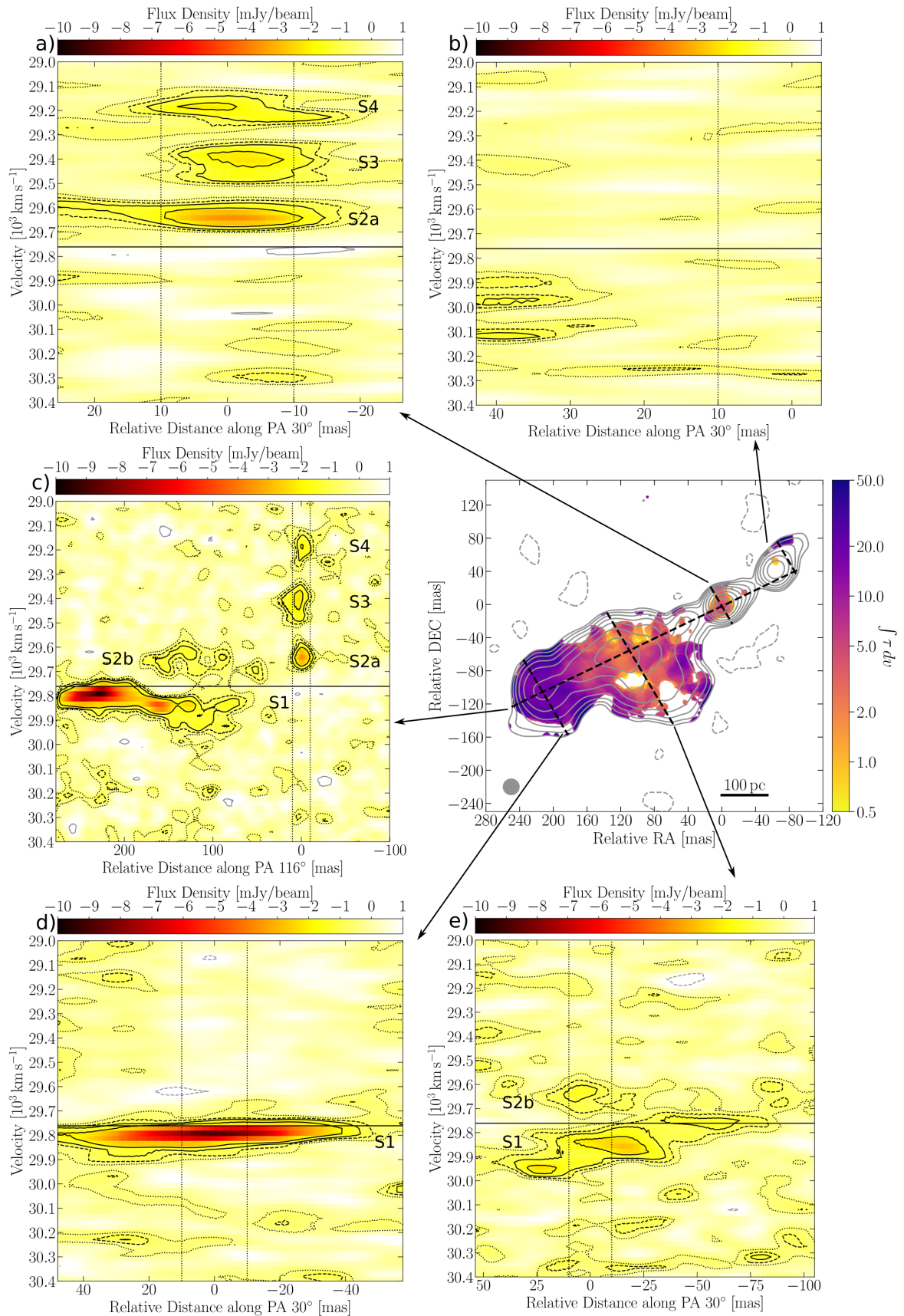


Fig. 4. Position-velocity plots (panels a to e) from 29000–34000 km s^{-1} for slices along different position angles. The same colour scale is applied to all position-velocity plots. The black dashed vertical lines mark the size of the synthesized beam for comparison, while the black solid horizontal line refers to the systemic velocity from [Labiano et al. \(2013\)](#). The black contour lines correspond to -1 (dotted lines), -2 (dashed lines), -3 and -5 (solid lines) times $\sigma_{\text{VLBI,cube}}$, while the solid gray contour line is set to $3\sigma_{\text{VLBI,cube}}$. The central panel shows the slices and the optical depth integrated over the same velocity range as the position-velocity plots, but including only channels with $\leq -3\sigma_{\text{VLBI,cube}}$.

4.1.1. Properties of the outflowing H I gas

Figure 5 shows the column density N_{H} normalized by the spin temperature T_{spin} following $N_{\text{H}} T_{\text{spin}}^{-1} \approx 1.823 \times 10^{18} \int \tau(v) dv \text{ cm}^{-2} \text{ K}^{-1}$, where v is in units of km s^{-1} . Again, we focus on the velocity range of $\sim 29000 \text{ km s}^{-1}$ to $\sim 30400 \text{ km s}^{-1}$ considering only channels with $\leq -3\sigma_{\text{VLBI, cube}}$. The spin temperature of the H I gas is unknown in 3C 236. However, it is very likely that it reaches higher values in the nuclear region than in the south-east lobe. A similar argument was made by Morganti et al. (2005a) and a T_{spin} of $\sim 1000 \text{ K}$ is often used for gas close to the active nucleus or gas with extremely disturbed kinematics, although measurements of this quantity are scarce (see Morganti et al. 2016; Holt et al. 2006). Thus, it seems reasonable to assume $T_{\text{spin}} = 1000 \text{ K}$ for S2a, S3 and S4 and $T_{\text{spin}} = 100 \text{ K}$ for S2b. This results in column densities of $1.8\text{--}4.0 \times 10^{21} \text{ cm}^{-2}$ for the clouds co-spatial to the nucleus and $1.8 \times 10^{20} \text{ cm}^{-2}$ for S2b (see Table 3).

We can further estimate the mass outflow rate $\dot{M}_{\text{H I}}$ following Heckman (2002)

$$\dot{M}_{\text{H I}} \sim 30 \frac{r_{\star}}{\text{kpc}} \frac{N_{\text{H}}}{10^{21} \text{ cm}^{-2}} \frac{v}{300 \text{ km s}^{-1}} \frac{\Omega}{4\pi} M_{\odot} \text{ yr}^{-1} \quad (1)$$

where r_{\star} is the distance of the cloud, v its velocity and Ω its solid angle which is assumed to be π . We estimate v for each of the features relative to the peak velocity of S1 (see Fig. 4c) and assume that r_{\star} is given by the size of the beam. The only exception is S2b for which we measure a distance of $\sim 150 \text{ mas}$ in Fig. 4c leading to $r_{\star} \sim 310 \text{ kpc}$ (de-projected). The resulting values are listed in Table 3. As both N_{H} and r_{\star} are lower limits, the actual mass outflow produced by these features is likely to be higher. Due to the order-of-magnitude lower column density compared to the clouds co-spatial to the nucleus, S2b has the lowest value. This is also the case for the density of all four clouds which ranges from $30\text{--}50 \text{ cm}^{-3}$ for S2a, S3 and S4 compared to 2 cm^{-3} for S2b (Table 3). For the former clouds a spherical geometry was assumed and for the latter an ellipsoidal geometry.

Morganti et al. (2005b) estimated the total mass outflow rate to be $\sim 47 M_{\odot} \text{ yr}^{-1}$ based on the full extent of the unresolved H I absorption spectrum ($v \sim 1500 \text{ km s}^{-1}$) and assuming an homogeneous distribution of the gas over a radius of 0.5 kpc . Thus, we consider this value an upper limit on the total mass outflow rate. Integrating over S2a, S3 and S4 yields $N_{\text{H}} \sim 7.8 \times 10^{21} \text{ cm}^{-2}$ and $\dot{M}_{\text{H I}} \sim 5 M_{\odot} \text{ yr}^{-1}$. This suggests that at least 10% of the estimated total mass outflow rate is located close (in projection) to the nucleus.

Following Holt et al. (2006), the kinetic energy of an outflow is given by

$$E_{\text{kin}} \approx 6.34 \times 10^{35} \frac{\dot{M}}{2} \left(v_{\text{out}}^2 + \frac{\text{FWHM}^2}{1.85} \right) \quad (2)$$

where FWHM is the full width at half maximum of the line. Labiano et al. (2013) fitted three Gaussian distributions to the H I WSRT spectrum. One of the distributions described the broad, blue wing of the spectrum with the following parameters: $v_{\text{hel}} = 29474 \text{ km s}^{-1}$ and $\text{FWHM} \sim 1100 \text{ km s}^{-1}$. Using these values and $\dot{M}_{\text{H I, max}} \sim 47 M_{\odot} \text{ yr}^{-1}$ yields $E_{\text{kin}} \sim 9.4 \times 10^{42} \text{ erg s}^{-1}$. The estimated mass of the central supermassive black hole of 3C 236 is $\log m_{\text{SMBH}} \approx 8.5 M_{\odot}$ (Mezcua et al. 2011) and implies that the maximum kinetic energy of the H I outflow is up to 0.02%

of the Eddington luminosity. For the VLBI detected outflow, we take the integrated mass outflow rate ($\geq 5 M_{\odot} \text{ yr}^{-1}$), the central velocity of S3 and the full width at zero intensity (FWZI) of 500 km s^{-1} (Fig. 4c). This suggests that the outflow close to the nucleus has at least 4% of the maximum kinetic energy.

Recent numerical simulations of jet interaction with an inhomogeneous multi-phase ISM have reached resolutions which allow a comparison with VLBI measurements (by e.g., Wagner et al. 2012; Mukherjee et al. 2016, 2017; Cielo et al. 2018). This allows us to qualitatively consider the implications for our measurements. In general, the simulations demonstrated the strong impact that powerful jets have on the velocity, temperature, pressure and density distribution of the ISM gas. When the jet hits the ISM, the gas at the shock front of the jet is being accelerated to the highest velocities. While the jet continues to push through the ISM, the already accelerated gas moves outwards along and transversal to the jet axis forming a kind of expanding cocoon around the jet. This disrupts the ISM in particular in the proximity of the jet and decreases the overall density of the gas. At some point the jet breaks through the ISM and the gas primarily expands transversal to the jet axis. However, the expansion of the jet can also be halted if the jet power is too low and/or the density of the medium is too high. This can prevent the jet from pushing all the way through the ISM. The velocities and densities of the clouds that we measure are within the range of values expected from these simulations. Given the properties of the clumpy H I gas and the morphology of the radio emission in 3C 236, it seems likely that we see the jet-H I interaction in an already advanced stage in its evolution. However, projection effects and the undetected H I gas make it difficult to assess whether the VLBI jet has already entirely pushed through the H I gas.

A more quantitative comparison is difficult as most of the available simulations consider only the warm and hot ISM gas ($\geq 10^4 \text{ K}$). An exception is the recent study by Mukherjee et al. (2018) of IC 5063 which traces the cold molecular gas down to 10^2 K . In contrast to 3C 236 the jet axis in IC 5063 is aligned with the disk. In this particular work, the simulations were able to reconstruct kinematic features of the cold gas as seen in observations by Morganti et al. (2015). Numerical simulations like the one performed by Mukherjee et al. (2018) are essential to understand the interaction of the radio jet and cold ISM gas.

4.2. The disk-related H I gas

Struve & Conway (2012) related the rather symmetric gradient around the deep absorption to a disk of H I gas (see Fig. 4d). They did not consider the gas detected within a distance of $< 200 \text{ mas}$ from the nucleus to be connected to it due to the lack of spatial and kinematic structure. However, our observations reveal a velocity gradient also across the central part of the lobe (Fig. 4d). It is larger than the one at the location of the deep absorption (Fig. 4a). Because the absorption extends to the edges of the continuum and not all of the absorption is recovered, it is difficult to measure the full width of the disk. Thus, we do not calculate the properties of the disk at this point as it would require more detailed modelling that is beyond the scope of this work.

The column density of the H I gas changes significantly across the lobe. Figure 5d depicts the gas related to S1. Struve & Conway (2012) reported a value of $N_{\text{H I}} \approx 6.1 \times 10^{21} \text{ cm}^{-2}$ at the location of the peak of the absorption assuming a conservative value of $T_{\text{spin}} = 100 \text{ K}$. This is similar to our measurements, but we find that there is variation over an order of magnitude across the lobe. The H I column densities are up to an order of

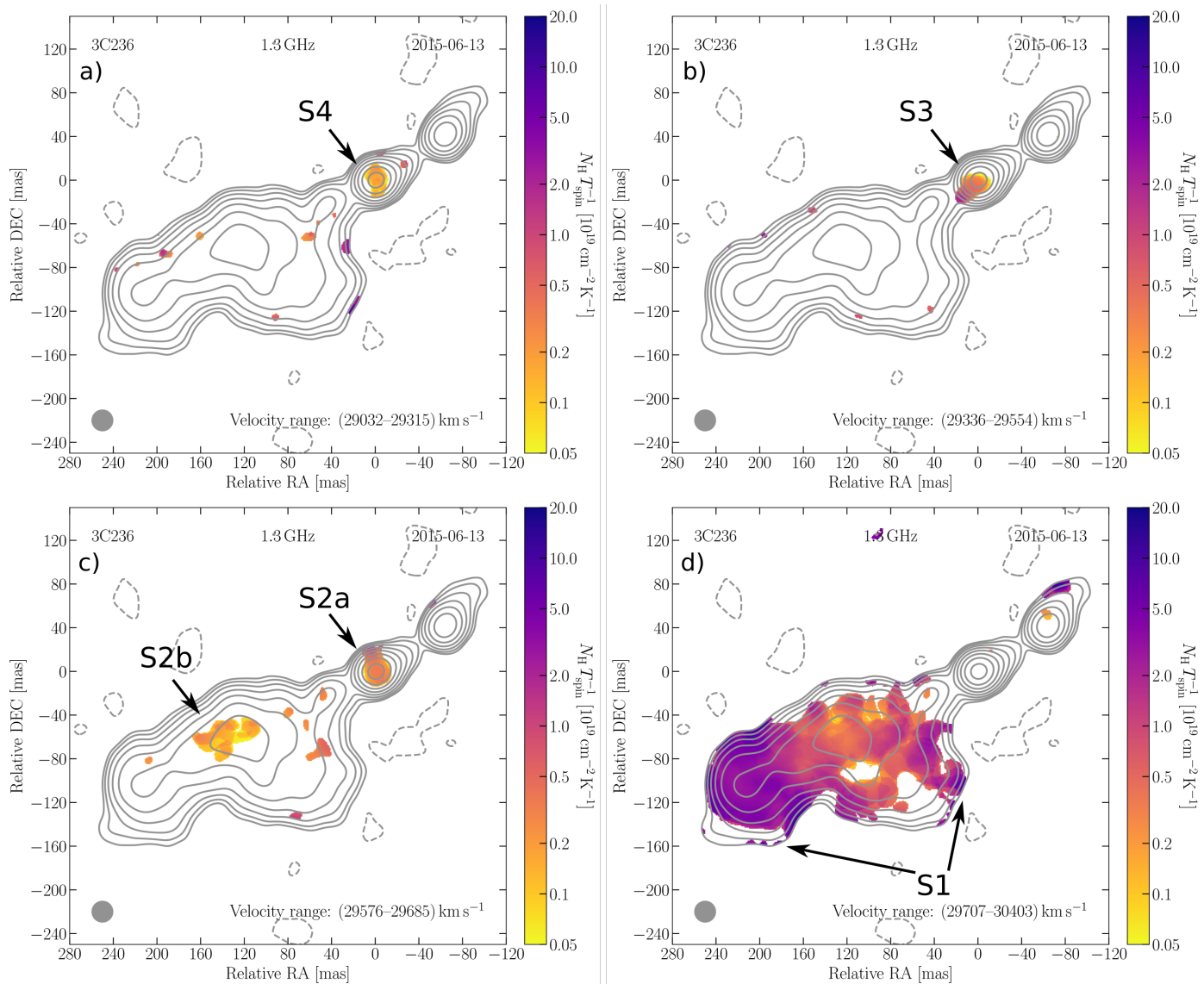


Fig. 5. Maps of $N_{\text{HI}} T_{\text{spin}}^{-1}$ for the features S1, S2a/b, S3 and S4 with the same logarithmic colour scale applied to all images. The velocity range is given in the bottom right corner and was chosen based on velocity range of the features in Fig. 4. The background shows the continuum map with contours beginning at $3\sigma_{\text{VLBI}}$ and increasing logarithmically by a factor of two. The grey circle in the lower left corner depicts the synthesized beam

magnitude lower than the column density from CO estimated by Labiano et al. (2013).

Assuming that the H I disk is aligned with the inner dust lane, we can estimate the height of the H I disk using the extent of S1 in Fig. 4c. This yields ≥ 200 mas or ≥ 360 pc in projection and has to be considered a lower limit due to the undetected H I gas. Schilizzi et al. (2001) estimated an apparent inclination of the radio jet to the line of sight of $\sim 60^\circ$ based on the ellipticity of the host galaxy and assuming that the jets are perpendicular to the dust lanes. This yields a de-projected height of the H I disk of ≥ 420 pc. The major axis of the inner dust line is about 1.8 kpc in projected size O’Dea et al. (2001) and the CO disk extends up to about 1.3 kpc. Assuming that the H I disk has the radial extent of the CO implies a thick rather than a thin disk. Nesvadba et al. (2011) also suggested an ellipsoidal configuration instead of thin disk for the H₂ gas on larger scales.

The distribution of the gas across the south-east radio lobe seen in our VLBI image and in Struve & Conway (2012) in addition to the co-spatiality with the inner dust lane provides

further support for the interpretation that the morphology of the lobe is, to some extent, the result of interaction between the jet and the dust lane (O’Dea et al. 2001). Such an interaction would affect the morphology and kinematics of the H I disk. The location and kinematic properties of S2b (see Fig. 4c,d and Fig. 5d) could be a signature of this interaction instead of being related to outflowing gas. In this context, it is interesting that Labiano et al. (2013) required two Gaussian functions to fit the deep part of the absorption spectrum, a deep, narrow component ($v_{\text{hel}} = 29828$ km s⁻¹, FWHM ~ 80 km s⁻¹) and a shallower, broader one ($v_{\text{hel}} = 29846$ km s⁻¹, FWHM ~ 300 km s⁻¹). Further investigations are necessary and would require detailed numerical simulations of the interaction between jet and the cold ISM.

4.3. Comparison with 4C 12.50

As mentioned in Sect. 1 the compact radio galaxy 4C 12.50 located at a redshift of 0.1217 is currently the only other powerful

Table 3. Properties of the kinematically disturbed HI clouds

Component ^a	$N_{\text{HI}} T_{\text{spin}}^{-1}$ ^b [$10^{19} \text{ cm}^{-2} \text{ K}^{-1}$]	N_{HI} ^c [10^{19} cm^{-2}]	d ^d [pc]	n_{HI} ^e [cm^{-3}]	m_{HI} ^f [$10^4 M_{\odot}$]	v ^g [km s^{-1}]	r_{\star} ^h [pc]	\dot{M}_{HI} ⁱ [$M_{\odot} \text{ yr}^{-1}$]
S4	0.18	18	$\lesssim 36$	30	0.65	640	$\lesssim 40$	1.2
S3	0.40	40	$\lesssim 36$	60	1.5	420	$\lesssim 40$	1.7
S2a	0.33	33	$\lesssim 36$	50	1.2	150	$\lesssim 40$	0.5
Nucleus	0.78	78	$\lesssim 36$	120	2.8	640	$\lesssim 40$	5
S2b	0.18	1.8	56×15	2	0.28	150	310	0.2

Notes. ^(a) Label of the kinematic component (see Fig. 4). The values for ‘Nucleus’ were obtained after integrating over S2a, S3, and S4 ^(b) H I column density normalised by spin temperature ^(c) H I column density. For S4, S3, and S2a $T_{\text{spin}} = 1000 \text{ K}$ is assumed, while for S2b $T_{\text{spin}} = 100 \text{ K}$ is assumed. ^(d) Projected size of the components. For S2a, S3, and S4 a spherical geometry is assumed with the major and minor axis given. ^(e) Density of the H I clouds. The same T_{spin} -values as for the column density are assumed here. ^(f) Mass of the H I clouds for the chosen T_{spin} -values. ^(g) Peak velocity of the H I clouds relative to the peak velocity of S1. ^(h) De-projected distance of the H I clouds relative to the nucleus ⁽ⁱ⁾ Mass outflow rate following Heckman (2002) for the chosen T_{spin} -values.

radio galaxy for which the H I outflow has also been studied with VLBI. There have been other radio galaxies in which a strong H I outflow has been detected and partially resolved, i.e., 3C 305 (Morganti et al. 2005a), 3C 293 (Mahony et al. 2013). However, these observations were obtained at lower angular resolution and thus probed larger spatial scales. Therefore, we focus our comparison on 4C 12.50.

Morganti et al. (2013) show that the H I gas is distributed on either end of its projected 200 pc-size radio structure, i.e., the deep absorption is located at the northern extent of the source, while the broad outflow is co-spatial with the hot spot in the southern part of the source. In contrast to 3C 236, no absorption was reported in the nuclear region and the high- and low-resolution H I spectrum match well which suggests that all of the absorption has been recovered by the VLBI observation.

Morganti et al. (2013) measured a column density of the blue-shifted clouds in 4C 12.50 of $4.6 \times 10^{21} \text{ cm}^{-2}$, using $T_{\text{spin}} = 100 \text{ K}$ due to the distance of the H I gas to the nucleus. This is comparable to S2a, S3 and S4 even though these are located co-spatial to the nucleus, i.e., a higher value for T_{spin} was assumed. The mass outflow rate of the H I in 4C 12.50 was determined to range between $16 M_{\odot} \text{ yr}^{-1}$ and $29 M_{\odot} \text{ yr}^{-1}$. However, it is difficult to compare with 3C 236 as we only measure lower limits. Although S2b would be better suitable for comparison in terms of its location, its column density and total H I mass is an order of magnitude lower than what was determined for 4C 12.50. The mass outflow rate and outflow velocity suggests a kinetic energy of about 0.02–0.03% of the Eddington luminosity for 4C 12.50 depending also on the assumed black hole mass (Dasyra et al. 2006, 2011; Son et al. 2012). This value range is similar to what we have estimated as a possible upper limit for the kinetic energy of the outflow in 3C 236. There is also potentially a large difference in the total H I mass. Morganti et al. (2013) estimated a mass of $\sim 1.4 \times 10^5 M_{\odot}$ for 4C 12.50 which represents a lower limit as the H I gas could be distributed beyond the radio continuum. Struve & Conway (2012) derived a value of $5.9\text{--}9 \times 10^9 M_{\odot}$ assuming the H I at the southern end of the lobe in 3C 236 is contained within a regular rotating disk.

The differences observed between these two objects can be the result of a combination of differences in size and age of the two sources and differences in the conditions of the ISM. The gas in 3C 236 could be more settled than in 4C 12.50. This may suggest that at the distances of the south-east radio lobe of 3C 236 of from the nuclear region of about 0.3 kpc, there are no more dense clouds and the jet has already broken through the denser

gas. This would open the possibility that both sources represent different stages of evolution at least with respect to the jet-H I interaction. 3C 236 could be further advanced in its evolution than 4C 12.50. The age of both radio sources have been estimated based on cooling time to be $\sim 10^4$ years (4C, 12.50, Morganti et al. 2013) and $\sim 10^5$ years (3C 236, O’Dea et al. 2001; Tremblay et al. 2010). The jet in 3C 236 could have had more time to interact with the H I dispersing the gas to greater extent. Thus, the combination of these parameters need to be considered when the presence (or absence) of outflows and their properties are investigated.

5. Summary & Conclusion

In this paper, we have presented results on the H I gas distribution in the central 1 kpc of the radio source 3C 236 as detected in absorption by milli-arcsecond global VLBI and arc-second VLA observations. We find that all of the H I gas recovered by VLBI is contained within the nuclear region and the south-east lobe of the radio source. The VLBI data recovers a significant amount of absorption from the disk-related and the outflowing H I gas component compared to the lower resolution VLA data as well as about 40% of the continuum flux density. The latter implies substantial extended low-surface brightness emission that is resolved out by the high resolution of VLBI.

For the first time, we have been able to localise part of the broad blue-shifted component of the H I gas in 3C 236 in the form of distinct clouds located almost exclusively in the compact nuclear region which is $\lesssim 40 \text{ pc}$ in size (in projection). The clouds cover a velocity range of about 600 km s^{-1} with respect to the peak of the disk-related H I gas and we estimate that they have a density of $\gtrsim 60 \text{ cm}^{-3}$. There is also one cloud co-spatial to the south-east lobe and well aligned with the position angle of the jet that appears to be kinematically disturbed gas. While it could be part of the H I disk, it is also possible that it resembles outflowing H I gas. In the latter case, its location and extended size implies a density as low as $\sim 2 \text{ cm}^{-3}$. Overall, the mass outflow rate of the VLBI detected outflowing gas is about 10% of the total mass outflow rate of $47 M_{\odot} \text{ yr}^{-1}$ estimated from unresolved spectra. The clouds co-spatial to the nuclear region account for about 4% of the total kinetic energy of the H I outflow. Because 3C 236 is classified as a LERG, we consider the radio jets as the most likely driver of the outflow.

The discrepancy between the low- and high-resolution H I absorption spectra in combination with the distribution of the

detected gas implies that both the observed and undetected H I outflow is clumpy. However, we cannot exclude the possibility of a highly diffuse gas component. A qualitative comparison with numerical simulations suggests that the interaction of the jet with the H I gas has already been going on for long time in 3C 236. In this scenario the high-velocity gas that we do not detect has been dispersed significantly as a result of the jet interaction. Even the disk-related H I gas could have been affected.

We compare our results 3C 236 to 4C 12.50, in which no absorption was detected co-spatial to the nuclear region and all of the H I was recovered by VLBI including the jet-driven outflowing gas. The differences to 3C 236 are very intriguing as it could be a sign that the gas is more settled in 3C 236. However, the available data does not allow to draw strong conclusions on whether both sources represent different stages in AGN evolution. Additional data on other sources are required.

This work is part of our ongoing effort to spatially resolve the jet-driven H I outflow in young and re-started powerful radio galaxies. It demonstrates that great care is required when physical quantities such as density and mass of the gas are derived from unresolved spectra. This shows the need for high-resolution follow-up observations of upcoming large H I absorption surveys conducted by e.g., Apertif (Oosterloo et al. 2010; Maccagni et al. 2017), MeerKat (Gupta et al. 2017), and ASKAP (Allison et al. 2015).

Acknowledgements. RS gratefully acknowledge support from the European Research Council under the European Union's Seventh Framework Programme (FP/2007-2013)/ERC Advanced Grant RADIOLIFE-320745. EKM acknowledges support from the Australian Research Council Centre of Excellence for All-sky Astrophysics (CAASTRO), through project number CE110001020. The European VLBI Network is a joint facility of independent European, African, Asian, and North American radio astronomy institutes. Scientific results from data presented in this publication are derived from the following EVN project code: GN002. The National Radio Astronomy Observatory is a facility of the National Science Foundation operated under cooperative agreement by Associated Universities, Inc. The Long Baseline Observatory is a facility of the National Science Foundation operated under cooperative agreement by Associated Universities, Inc. The Arecibo Observatory is a facility of the National Science Foundation (NSF) operated by SRI International in alliance with the Universities Space Research Association (USRA) and UMET under a cooperative agreement. The Arecibo Observatory Planetary Radar Program is funded through the National Aeronautics and Space Administration (NASA) Near-Earth Objects Observations program. Based on observations made with the NASA/ESA Hubble Space Telescope, and obtained from the Hubble Legacy Archive, which is a collaboration between the Space Telescope Science Institute (STScI/NASA), the Space Telescope European Coordinating Facility (ST-ECF/ESA) and the Canadian Astronomy Data Centre (CAD/C/NRC/CSA). This research has made use of NASA's Astrophysics Data System Bibliographic Services. This research has made use of the NASA/IPAC Extragalactic Database (NED) which is operated by the Jet Propulsion Laboratory, California Institute of Technology, under contract with the National Aeronautics and Space Administration. This research made use of Astropy, a community-developed core Python package for Astronomy (Astropy Collaboration et al. 2013). This research made use of APLpy, an open-source plotting package for Python Robitaille & Bressert (2012).

References

- Alexander, D. M. & Hickox, R. C. 2012, *New A Rev.*, 56, 93
Allison, J. R., Sadler, E. M., Moss, V. A., et al. 2015, *MNRAS*, 453, 1249
Araya, E. D., Rodríguez, C., Pihlström, Y., et al. 2010, *AJ*, 139, 17
Associated Universities, I. 1999, AIPS: Astronomical Image Processing System, Astrophysics Source Code Library
Astropy Collaboration, Robitaille, T. P., Tollerud, E. J., et al. 2013, *A&A*, 558, A33
Barthel, P. D., Miley, G. K., Jagers, W. J., Schilizzi, R. T., & Strom, R. G. 1985, *A&A*, 148, 243
Best, P. N. & Heckman, T. M. 2012, *MNRAS*, 421, 1569
Böck, M. 2012, PhD thesis, Friedrich-Alexander-Universität Erlangen-Nürnberg, Erlangen, Germany
Buttiglione, S., Capetti, A., Celotti, A., et al. 2010, *A&A*, 509, A6
Carilli, C. L., Wrobel, J. M., & Ulvestad, J. S. 1998, *AJ*, 115, 928
Ciolo, S., Bieri, R., Volonteri, M., Wagner, A. Y., & Dubois, Y. 2018, *MNRAS*, 477, 1336
Condon, J. J., Cotton, W. D., Greisen, E. W., et al. 1998, *AJ*, 115, 1693
Croton, D. J., Springel, V., White, S. D. M., et al. 2006, *MNRAS*, 365, 11
Dasra, K. M., Ho, L. C., Netzer, H., et al. 2011, *ApJ*, 740, 94
Dasra, K. M., Tacconi, L. J., Davies, R. I., et al. 2006, *ApJ*, 638, 745
Di Matteo, T., Springel, V., & Hernquist, L. 2005, *Nature*, 433, 604
Fabian, A. C. 2012, *ARA&A*, 50, 455
Geréb, K., Maccagni, F. M., Morganti, R., & Oosterloo, T. A. 2015, *A&A*, 575, A44
Gupta, N., Srianand, R., Baan, W., et al. 2017, *ArXiv e-prints* [arXiv:1708.07371]
Harrison, C. M. 2017, *Nature Astronomy*, 1, 0165
Heckman, T. M. 2002, in *Astronomical Society of the Pacific Conference Series*, Vol. 254, *Extragalactic Gas at Low Redshift*, ed. J. S. Mulchaey & J. T. Stocke, 292
Heckman, T. M. & Best, P. N. 2014, *ARA&A*, 52, 589
Hill, G. J., Goodrich, R. W., & Depoy, D. L. 1996, *ApJ*, 462, 163
Högbom, J. A. 1974, *A&AS*, 15, 417
Holt, J., Tadhunter, C., Morganti, R., et al. 2006, *MNRAS*, 370, 1633
International Consortium Of Scientists. 2011, *CASA: Common Astronomy Software Applications*, Astrophysics Source Code Library
Kormendy, J. & Ho, L. C. 2013, *ARA&A*, 51, 511
Kunert-Bajraszewska, M., Gawroński, M. P., Labiano, A., & Siemiginowska, A. 2010, *MNRAS*, 408, 2261
Labiano, A., García-Burillo, S., Combes, F., et al. 2013, *A&A*, 549, A58
Maccagni, F. M., Morganti, R., Oosterloo, T. A., Geréb, K., & Maddox, N. 2017, *A&A*, 604, A43
Mahony, E. K., Morganti, R., Emonts, B. H. C., Oosterloo, T. A., & Tadhunter, C. 2013, *MNRAS*, 435, L58
McNamara, B. R. & Nulsen, P. E. J. 2007, *ARA&A*, 45, 117
Meyer, M., Robotham, A., Obreschkow, D., et al. 2017, *PASA*, 34 [arXiv:1705.04210]
Mezcua, M., Lobanov, A. P., Chavushyan, V. H., & León-Tavares, J. 2011, *A&A*, 527, A38
Morganti, R. 2017, *Frontiers in Astronomy and Space Sciences*, 4, 42
Morganti, R., Fogasy, J., Paragi, Z., Oosterloo, T., & Orienti, M. 2013, *Science*, 341, 1082
Morganti, R., Oosterloo, T., Oonk, J. B. R., Frieswijk, W., & Tadhunter, C. 2015, *A&A*, 580, A1
Morganti, R., Oosterloo, T., & Tsvetanov, Z. 1998, *AJ*, 115, 915
Morganti, R., Oosterloo, T. A., Tadhunter, C. N., van Moorsel, G., & Emonts, B. 2005a, *A&A*, 439, 521
Morganti, R., Tadhunter, C. N., & Oosterloo, T. A. 2005b, *A&A*, 444, L9
Morganti, R., Veilleux, S., Oosterloo, T., Teng, S. H., & Rupke, D. 2016, *A&A*, 593, A30
Mukherjee, D., Bicknell, G. V., Sutherland, R., & Wagner, A. 2016, *MNRAS*, 461, 967
Mukherjee, D., Bicknell, G. V., Sutherland, R., & Wagner, A. 2017, *MNRAS*, 471, 2790
Mukherjee, D., Wagner, A. Y., Bicknell, G. V., et al. 2018, *MNRAS*, 476, 80
Nesvadba, N. P. H., Boulanger, F., Lehnert, M. D., Guillard, P., & Salome, P. 2011, *A&A*, 536, L5
Nyland, K., Young, L. M., Wrobel, J. M., et al. 2016, *MNRAS*, 458, 2221
O'Dea, C. P. 1998, *PASP*, 110, 493
O'Dea, C. P., Koekemoer, A. M., Baum, S. A., et al. 2001, *AJ*, 121, 1915
Oosterloo, T., Verheijen, M., & van Cappellen, W. 2010, in *ISKAF2010 Science Meeting*, 43
Oosterloo, T. A., Morganti, R., Tzioumis, A., et al. 2000, *AJ*, 119, 2085
Orienti, M. 2016, *Astronomische Nachrichten*, 337, 9
Peck, A. B. & Taylor, G. B. 2001, *ApJ*, 554, L147
Peck, A. B., Taylor, G. B., & Conway, J. E. 1999, *ApJ*, 521, 103
Perley, R. A. & Butler, B. J. 2013, *ApJS*, 204, 19
Robitaille, T. & Bressert, E. 2012, APLpy: Astronomical Plotting Library in Python, Astrophysics Source Code Library
Sault, R. J., Teuben, P., & Wright, M. C. H. 2011, *MIRIAD: Multi-channel Image Reconstruction, Image Analysis, and Display*, Astrophysics Source Code Library
Sault, R. J., Teuben, P. J., & Wright, M. C. H. 1995, in *Astronomical Society of the Pacific Conference Series*, Vol. 77, *Astronomical Data Analysis Software and Systems IV*, ed. R. A. Shaw, H. E. Payne, & J. J. E. Hayes, 433
Schilizzi, R. T., Tian, W. W., Conway, J. E., et al. 2001, *A&A*, 368, 398
Shepherd, M. 2011, *Difmap: Synthesis Imaging of Visibility Data*, Astrophysics Source Code Library
Shepherd, M. C., Pearson, T. J., & Taylor, G. B. 1994, in *BAAS*, Vol. 16, *BAAS*, 987–989
Silk, J. & Rees, M. J. 1998, *A&A*, 331, L1
Son, D., Woo, J.-H., Kim, S. C., et al. 2012, *ApJ*, 757, 140
Struve, C. & Conway, J. E. 2010, *A&A*, 513, A10

- Struve, C. & Conway, J. E. 2012, *A&A*, 546, A22
- Tadhunter, C. 2016, *A&A Rev.*, 24, 10
- Taylor, G. B., Hough, D. H., & Venturi, T. 2001, *ApJ*, 559, 703
- Tremblay, G. R., O’Dea, C. P., Baum, S. A., et al. 2010, *ApJ*, 715, 172
- van Gorkom, J. H., Knapp, G. R., Ekers, R. D., et al. 1989, *AJ*, 97, 708
- Veilleux, S., Cecil, G., & Bland-Hawthorn, J. 2005, *ARA&A*, 43, 769
- Vermeulen, R. C., Labiano, A., Barthel, P. D., et al. 2006, *A&A*, 447, 489
- Vermeulen, R. C., Ros, E., Kellermann, K. I., et al. 2003, *A&A*, 401, 113
- Wagner, A. Y., Bicknell, G. V., & Umemura, M. 2012, *ApJ*, 757, 136
- Wagner, A. Y., Bicknell, G. V., Umemura, M., Sutherland, R. S., & Silk, J. 2016, *Astronomische Nachrichten*, 337, 167
- Willis, A. G., Strom, R. G., & Wilson, A. S. 1974, *Nature*, 250, 625